# Are Laboratory-Formed Hydrate-Bearing Systems Analogous to Those in Nature?

Erik Spangenberg,* Mike Priegnitz, Katja Heeschen, and Judith M. Schicks

*Helmholtz Centre Potsdam GFZ German Research Centre for Geosciences, Telegrafenberg, 14473 Potsdam, Germany

ABSTRACT: The intensive study of hydrate-bearing sandy sediments, a possible source of fossil energy for future generations, leads to an accumulation of information from field studies, laboratory studies, and modeling. This information is used to create conceptual models for hydrate deposit genesis helping to assess the value of laboratory experimental studies on artificially formed hydrate-bearing sediments. We present an experimental example on the simulation of hydrate formation from methane dissolved in water, which is assumed to be the most likely natural process for the genesis of highly concentrated hydrate in sandy sediments. Measurements of the concentration of dissolved methane, temperature, and electrical resistivity tomography are used to describe and characterize the hydrate formation process. It could be shown that the way in which hydrate forms in this laboratory experiment corresponds to the procedure assumed for natural scenarios. The main difference to nature is probably the high crystal growth rate which seems to result in an increased water−hydrate interface and a subsequent "aging" or recrystallization process affecting certain physical properties.

hydrate formation - from lab to reservoir
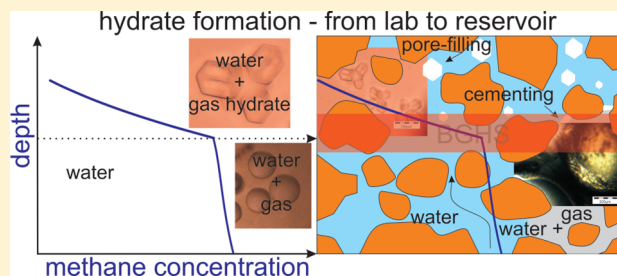
1. INTRODUCTION

Gas hydrates are nonstoichiometric crystalline solids composed of low molecular weight gases that are encased in a lattice of hydrogen-bonded water molecules.[1] Hydrates are stable under conditions of elevated pressure and low temperature given appropriate gas concentrations and water supply. In natural environments, they preferentially occur as methane hydrate in seafloor sediments and beneath the permafrost in arctic regions.[2,3] Since a number of estimates suggest that large amounts of carbon are stored in naturally occurring methane hydrates,[4,5] these deposits have attracted interest as a possible future energy resource.[6−8] Hydrates occur primarily as massive solid bodies in association with gas venting,[9] as grain-displacing aggregations (nodules and veins) in poorly compacted fine-grained sediments,[10,11] and as pore-filling gas hydrates with hydrate saturations less than 10 % in fine-grained sediments and much higher saturations (50 % to 90 %) in coarser materials such as coarse silts and sands (see Boswell et al. and references therein).[12] An explanation for the different hydrate morphologies found in natural water-saturated hydrate systems can be provided by particle-level force analysis. The hydrate morphology is governed by skeleton and capillary forces, which depend on the burial depth and grain size of the host sediment.[13] Although current estimates suggest that only 10 % or even less of the gas bound to methane hydrate can be found in sand/sandstone formations,[14] this type of reservoir is the focus of exploration for hydrates as energy resource. The high permeability of sands compared to that of the fine-grained sediments is very likely the reason that hydrate can accumulate to concentrations up to 90 % of the available pore volume.[14−16] Furthermore, if the hydrate is destabilized by pressure reduction, heating, or injection of chemicals, the pores become

free and permeable to access further regions of the reservoir and to produce the released gas via the well bore with the existing technology of the oil and gas industry. Reservoir delineation, general reservoir properties, and migration pathways can be identified using geophysical methods such as seismic or electromagnetic surveys.[17−19] These mapping technologies rely on the influence that hydrate exerts on the physical properties of the sediment relative to those of the hydrate-free sediments.[20] The resistivity increases with increasing hydrate content because hydrate as a nonconducting phase replaces the conductive pore water. Modeling results show that the way in which hydrate influences the electrical properties depends on the hydrate habit and the location where the hydrate forms in the pore space.[21] The influences of nodular, layered, cementing, and noncementing pore-filling hydrate habits on the electrical properties were studied in detail. For noncementing pore-filling hydrate the model predicts a dependence of resistivity on hydrate saturation and grain-size. This influence on grain size becomes apparent for hydrate saturations higher than 60 %. This dependency results from the change of free-water-dominated conduction to bound-water-dominated conduction at higher hydrate concentrations and from the fact that the bound-water to free-water ratio depends on grain-size. Laboratory experiments seem to show such an effect already for lower hydrate concentrations.[22] However,
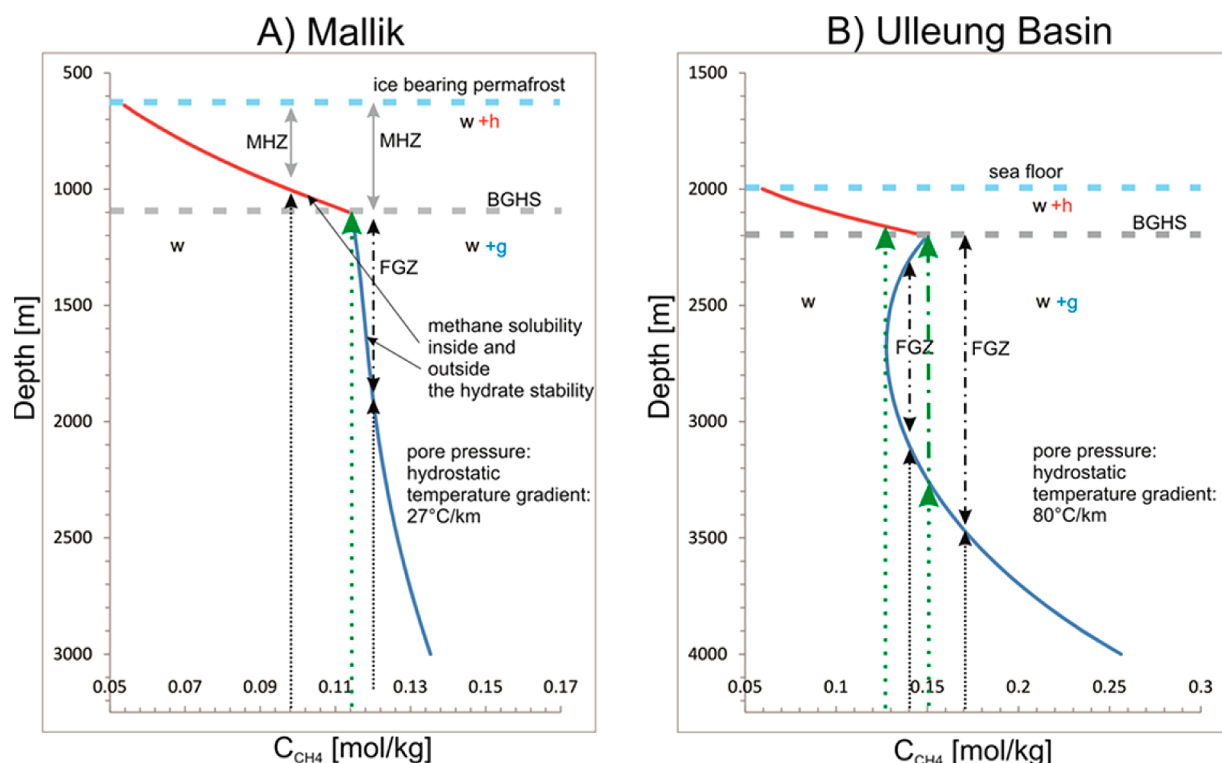
Figure 1. Solubility of methane in brine as a function of depth based on prevailing conditions at (A) the Mallik test site and (B) the Ulleung Basin (see text). The blue and red curves are the methane solubility curves in the absence (blue) and presence (red) of gas hydrate. They are based on equations published by Duan and Mao[36] and Sloan,[1] respectively. The arrows indicate advecting fluids with different methane concentrations, which become oversaturated when crossing the solubility curve (blue line) and migrate then as a two-phase system (dotted, liquid; dot−dashed, liquid + gas). FGZ, free-gas zone; MHZ, methane hydrate zone; BGHS, base of gas hydrate stability zone; w, water, h, hydrate, g, gas.

these models are not practical for the estimation of hydrate saturation from resistivity measurements. Hence, Archie's equation[23] is used to interpret electrical field measurements in coarse grained sediments, where the contribution from surface conductivity is negligible.[24]

For the seismic properties the situation is similar. Generally seismic velocities (p- and s-wave) increase with increasing hydrate content. How strong seismic velocities increase with hydrate saturation depends on the location where the hydrate forms in the pores. Generally three habits are distinguished for pore space hydrate in sands (see Waite et al. and references therein):[20] (1) noncementing pore-filling, (2) load bearing, and (3) cementing hydrate, which can be subdivided into grain-contact cementation and grain-coating cementation. Non-cementing pore-filling hydrate grows freely in the pore space without contact to the sediment grains. At a certain hydrate saturation (25 % to 40 %),[25,26] it starts to build bridges between neighboring grains and becomes load-bearing and grain-supporting, respectively. Another modeling approach avoids the consideration of different hydrate habits using the patchy saturation concept[27] to estimate the influence of hydrate saturation on physical rock properties.[13] Dai et al.[13] argue that in mature coarse grained hydrate systems Oswald ripening[28] of pore-filling hydrate will result in "patchy hydrate saturation" where patches containing 100 % hydrate in the pores are embedded in a hydrate-free water-saturated sand. For a detailed description of the modeling methodology see Dai et al.[13] and references therein.

However, there are a number of theoretical and semi-empirical models that relate physical properties to hydrate saturation while accounting for different hydrate pore habits

(e.g., Dvorkin et al. and Chand et al.).[29,30] The application of the existing rock physical models on field data does not fully meet the requirements. Dai et al.[17] state: "More work should be done to further refine the existing rock models as we access data from offshore regions. Controlled laboratory experiments will also add value, provided care is taken to simulate in the experiments the environment of the naturally occurring hydrates." This expresses the demand of geophysical explora-tion on petrophysics. Tackling this problem requires a better understanding of the geological controls on hydrate formation in porous systems, which can only be achieved by combining all sources of information: drilling, coring, logging, laboratory experiments, and modeling.

This paper aims to combine the increased knowledge available on hydrate bearing reservoirs from field studies, numerical studies on field scenarios, and conceptual models with laboratory measurements and observations on artificial hydrate-bearing sediment samples. The goal is an assessment of the value of laboratory studies with artificial samples to natural hydrate occurrences. Since concentrated hydrates in sands and coarse silts are moved into the focus of interest[14] and it is assumed that these reservoirs formed from dissolved-phase methane,[20,31] we will concentrate on the formation mechanism of hydrate from dissolved-phase methane in artificial laboratory samples. This will allow us to outline the experience gained with this method during the past few years.

2. CONCEPTUAL MODELS

2.1. The Formation of Hydrate-Bearing Sandy Reservoirs.
At the Mallik 38 L, 2 L, and 5 L research and production wells, hydrate has been found down to a depth of

about 1100 m.[16] On the basis of the hydrate stability calculations, the depth of the methane hydrate zone (MHZ) coincides with the base of gas hydrate stability (BGHS, defined by temperature and pressure); thus, the migrating pore water must be methane saturated when entering the BGHS (Figure 1A, green dotted arrow). Pore water with lower methane concentrations (dotted black arrow) would only become saturated at shallower depths leading to a shallower MHZ compared to the BGHS. Higher methane concentrations would then result in a free-gas zone (FGZ) directly below the BGHS. At a certain depth the pore water would reach saturation (dotted black arrow; the dotted signature represents single phase flow). With further decreasing depth a gas phase would evolve and migrate with the water as two-phase flow (dot-dashed black arrow; the dot-dash signature represents two phase flow). Despite very high gas hydrate saturations of up to 90 % in sands just above the BGHS (1107 m),[16] no free-gas-bearing sediment has been confirmed by well-log-analysis below the BGHS.[32]

In the Ulleung Basin the variation of methane solubility with depth is much stronger because of the high geothermal gradient (Figure 1B). It even has a local minimum below the BGHS at a depth of about 2700 m. As before, the left green dotted arrow marks the maximum CH_4 concentration which does not exceed the solubility limit before the water migrates into the BGHS. In this situation the dotted green arrow strikes the solubility limit inside the stability field, slightly above the BGHS. Water with a methane concentration of about 0.15 mol/kg, migrates along the right green arrow. The water crosses the solubility curve below its local minimum, and a free-gas phase will evolve and migrate together with the water (the green dot-dashed arrow marks the range of two-phase flow). For methane concentrations in between both green arrows (0.13 mol/kg < C_{CH_4} < 0.15 mol/kg) the upward migrating water crosses the solubility curve twice. For the first time at a depth below 2700 m the water becomes oversaturated and free gas will form, and for the second time, at a depth below the BGHS, the water will cross the solubility curve and start to dissolve the gas again. Theoretically, between the green arrows, the water could dissolve the available free gas completely and reach the BGHS as a methane-saturated single liquid phase. Depending on the relation between mass transport and dissolution kinetics, some free gas might reach the BGHS. In any case, a free-gas zone (FGH) exists below the BGHS, although the top of the FGZ might be separated by a certain distance from the BGHS (black arrow between the green arrows). Right from the second green arrow a free-gas zone exists directly beneath the BGHS (right black arrow). Ryu et al.[33] reported BSRs in some locations in the western deep water Ulleung Basin characterized by a sharp velocity increase above and a strong velocity decrease below the BGHS. The observed velocity decrease is a strong argument for the existence of free gas underlying the hydrates. For a more general view on methane transport into the hydrate stability zone see Rempel and Buffett[34] and Xu and Ruppel.[35]

Despite this conceptual model being rather simplified, it satisfies the derivation of different scenarios of methane transport into the MHZ and the resulting different hydrate formation mechanisms leading to different hydrate habits. To satisfy the high variability of natural systems, gas migration due to enhanced methane production, gas reservoirs, adsorption processes in clay-rich sediments, or other chromatographic separation of gases would need to be taken into account to

explain features such as the missing free-gas zone directly below the BGHS at the Mallik test site. An undersaturation of methane is not to be expected at this site from the concentration−depth function only since there is a conventional natural gas reservoir at greater depth,[37] which is assumed to be the source for the formation of the gas hydrate reservoirs above.

If methane is produced outside the stability field and migrates into the zone of hydrate stability, we can distinguish the following scenarios.

2.2. Scenario 1: Dissolved-Phase Methane Transport into the MHZ. If the migrating methane-laden pore water is undersaturated when entering the BGHS, it advects into colder regions before the solubility in the presence of gas hydrates is exceeded, which in turn leads to the growth of pore filling hydrates directly from the dissolved phase. The bottom of the MHZ would be located above the BGHS. If the saturation limit for dissolved methane was reached directly at the BGHS (see green dashed line in Figure 1A), hydrate would start to form directly at the BGHS which is then the bottom of the MHZ.

Figure 1 shows that the change of methane solubility with depth is strongest directly at the BGHS and slowly decreases with decreasing depth into the MHZ. Once hydrate is formed, it can be assumed that the highest hydrate formation rate and concentration occur directly above the bottom of the MHZ and both rate and concentration decrease with depth, since the change of solubility decreases (see explanation in section 3.3).

2.3. Scenario 2: Gas-Phase Methane Transport to the BGHS. If the methane concentration exceeds solubility before the pore water reaches the BGHS, methane gas bubbles will form in the pores. Small bubbles might be transported upward with the advecting pore water and grow due to the decreasing methane solubility and the decreasing pressure until they get trapped at grain surfaces and pore throats by capillary forces. They possibly form larger patches of gas filled pores before moving again, controlled by capillary effects involving interfacial tension, wettability of the solid surface, and the geometric structure of the interfaces.[38−40] Because the induction time for initial hydrate nucleation can be neglected on a geological time scale (see section 3.2 and 3.3) the free-gas phase reaching the BGHS, will immediately form hydrate at the gas−water interface and start sealing the BGHS (Figure 2 and Figure 3). If there is a two-phase flow of methane gas and water toward the BGHS, the migrating water is generally methane saturated and hydrate will form from gaseous and dissolved methane.

2.4. Scenario 3: Depth Shift of Stability Conditions Due to Sea Level or Climate Changes. The formation of
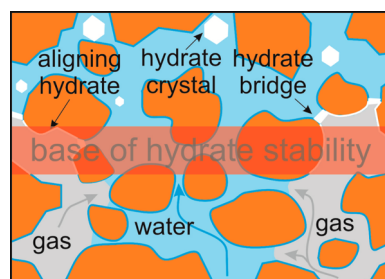
Figure 2. Sketch of a two-phase flow of methane-laden pore water and free methane gas into the MHZ. Hydrate forms at the water−gas interface, and from dissolved methane in the MHZ as it was observed in the laboratory experiments (see following sections).
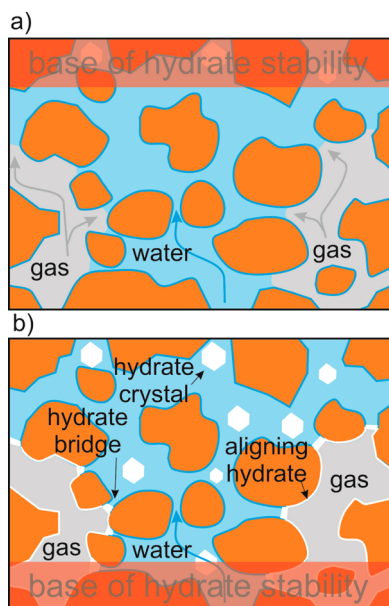
Figure 3. Free gas below the original BGHS (a) is shifted into the MHZ when the BGHS moves downward (b). At the gas—water interface grain-bridging hydrate and grain-aligning hydrate are formed, where noncementing pore-filling hydrate crystallizes from dissolved methane in the water filled pores and from microscopic gas bubbles.

methane hydrate can also result from the shift of the BGHS toward greater depths where sediments have substantial accumulations of free methane gas. This might result from a pressure increase due to a sea level rise[41] or a temperature decrease, for example, in conjunction with a progression of permafrost.[42]

If a sediment layer containing a high concentration of free methane gas is shifted into the MHZ by one of the above-described processes, hydrate formation from methane gas and pore water would occur throughout the gas-bearing sediment unit (Figure 3) and would not be restricted to the BGHS as in scenario 1. A high concentration of free gas in this scenario implies that the gas forms a continuous phase throughout the pore network over a large spatial area. The hydrate formation from methane gas and water would occur directly at the gas—water interface forming a "seal" that restricts the phase exchange to gas diffusion through the hydrate structure and temporary water leakage into the gas patch. Three phases would be present in the MHZ: liquid, gas, and gas hydrate.

In smaller isolated gas-saturated patches the pressure will decrease when the gas is consumed in the hydrate formation process. Because of the pressure difference over the "hydrate seal", water may leak into the patch until the gas is consumed. The life span of such an isolated patch depends on the volume of entrapped gas. In addition to such isolated gas compartments, gas-bearing areas might exist which are still connected to
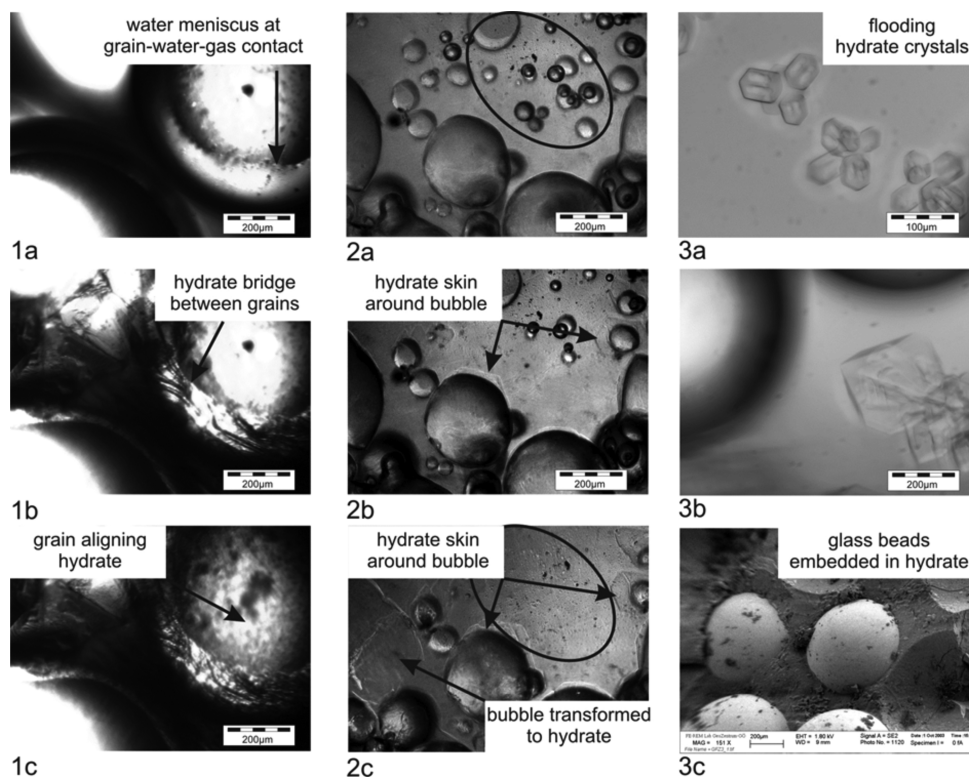
Figure 4. Images of hydrate growing from water and free methane gas (panels 1 and 2) and from methane dissolved in water (panels 3). The procedure to gain these photographs is described in detail in Spangenberg et al.[47] (1a) Glass beads, water, and methane situated outside the hydrate stability. (1b) Hydrate growing at the gas—water interface forming a bridge between neighboring grains. (1c) Water, wetting the glass beads is finally transformed into hydrate and the grain surface is covered with grain aligning hydrate. (2a) Methane bubbles in water outside the hydrate stability field. (2b) Within the hydrate stability field hydrate starts to form around the bubbles. (2c) Large bubbles are transformed to hydrate (some with a gas inclusion inside), whereas smaller bubbles disappear due to dissolution and hydrate formation (see ellipse in panels 2a and 2b). (3a) Hydrate formed from methane dissolved in water without a free-gas phase crystallizes in the pore water. (3b) To date there is no evidence that hydrate crystals grow at grain surfaces. We could only observe hydrate flooding in the pore water. (3c) An SEM-image of glass beads embedded in a matrix of almost pure methane hydrate (ice to hydrate ratio is 17 % to 83 %).[15]

the free-gas zone below the BGHS, for example, in conduits. These areas may be fed with methane gas from greater depth and could build up considerable overpressure across the hydrate barrier. The overpressure might lead to fracture formation and further gas invasion into or through the MHZ. For a detailed description of these processes see Fauria and Rempel.[40]

The residual water trapped inside the gas zones would be depleted owing to hydrate formation until the increasing salinity shifts the system to the three phase equilibrium.[4] The coexistence of gas hydrate and water with free gas in the MHZ is used as an explanation for the "wipe-out zones" observed in seismic surveys.[43]

If a sediment layer is shifted into the MHZ with a concentration of free gas too low to form a continuous gas phase, the gas occurs as microscopic bubbles in the pores, and will be consumed in hydrate formation as it enters the stability field. Another important aspect is the formation of various forms of gas hydrates such as noncementing pore-filling in the water saturated areas as well as grain-coating and grain-bridging hydrate in the gas compartments.

If the methane is formed by microbial activity inside the hydrate stability field, hydrate would form from methane dissolved in pore water. Microbial methane production generally is bound to organic-rich fine-grained sediments where a certain amount of "supersaturation" with respect to hydrate stability may occur because hydrate formation is inhibited in small pores.[44] The dissolved methane might diffuse into neighboring sandy sediments and form pore-filling hydrate.[45]

3. EXPERIMENTAL RESULTS AND DISCUSSION

3.1. Laboratory Observations Regarding the Specific Habitus of Gas Hydrates from Different Formation Scenarios. The visual observations from hydrate formation in laboratory studies (see Figure 4) support the following conception of the hydrate formation and growth process:

(i) Hydrate formation from gaseous methane is preferred at the gas–water interface (Figure 4 panels 1a to 1c and 2a to 2c). The specific shape of the gas–water interface results from the wetting properties, surface tension, and the pore space structure (grain shape and grain size distribution).

(ii) A hydrate film develops along the water–methane interface forming hydrate bridges in the pore throats between the grains and a shell of grain-aligning hydrate at the interface between the methane gas and the bound-water that wets the sediment grains (Figure 4 panels 1a to 1c; also see Freer et al.[46]). However, the hydrate formation at the gas–water–grain interface leads to barriers that could trap gas and restrict methane transport to diffusion through the hydrate barrier. Small gas bubbles might be dissolved and feed the growth of the hydrate around larger bubbles (Figure 4 panels 2a–2c).

(iii) Methane saturated water migrates into the hydrate stability zone where it cools down and hydrate crystals nucleate and grow from the excess methane and water since the methane solubility decreases with temperature (Figure 4 panels 3a–3c).

The grain-bridging and grain-coating hydrate habit shown in Figure 4 1b,1c results if hydrate is formed with sufficient gas to consume the available pore water completely. Transforming the water into hydrate by continuous gas supply to partially water-saturated sediment samples is used in a number of laboratory experimental studies.[48–50] This method, called "excess gas method", forms grain-cementing hydrate.[51] Laboratory formed

hydrate-bearing sediment samples of this type very likely reflect physical properties similar to hydrate-bearing sediments directly at the BGHS with underlying gas (scenario 2) and gas saturated areas within the MHZ (scenario 3).

Measurements show that only 5 % to 10 % hydrate saturation with cementing hydrate increases the seismic p-wave velocity as about 40 % of pore-filling hydrate.[51] Transferring this finding to scenario 2 would explain that strong BSRs could exist at a BGHS with underlying gas even if the hydrate saturation is low.

Figure 4 panels 2a to 2c show that microscopic gas bubbles are transformed into hydrate with time, if sufficient water is supplied. This is probably the way hydrates form in the "excess water method".[51] In this method, a known value of methane gas is injected into the specimen before water is injected until the target pore pressure is reached. The sample is cooled into the stability field and the pore pressure is held constant during hydrate formation by water injection.[51] This method results in a load-bearing or grain-supporting and pore-filling hydrate habit. This is probably what we can expect in scenarios 2 and 3, if the gas saturation in the sediments is low and the gas occurs as small bubbles in pores rather than as a continuous phase throughout the pore network before entering the hydrate stability field.

Figure 4 panels 3 show noncementing pore-filling hydrate formed from methane dissolved in water. Because methane solubility is low, hydrate formation from dissolved-phase methane in the laboratory is a slow and long-lasting process.[15,52,53] However, because it is assumed that this process forms the high hydrate concentrations in sands and coarse silts,[31,20] the method should be improved in order to provide information and data that are valuable for the interpretation of geophysical field and borehole measurements and the general understanding of this type of hydrate-bearing reservoirs. This formation process corresponds to scenario 1.

3.2. Formation of Laboratory Hydrate-Bearing Samples from Dissolved-Phase Methane. *Experimental System and Hydrate Formation Procedure.* A major drawback of the experimental system used for the generation of hydrate bearing samples in the studies of 2005 to 2007[15,47] was the small sample size. The sediment sample cell of this system was 50 mm in both diameter and length. In this small setup, it was difficult to exactly control the temperature right at the fluid inlet which made the system very susceptible to hydraulic clogging. On the basis of this methodological concept, a large reservoir simulator (LARS) was developed. Because great importance was placed on the temperature control directly at the fluid inlet, clogging can be avoided and hydrate can form in porous sediments from dissolved phase methane on a routine base.[52] The main five components of LARS are shown in Figure 5. Here we will focus on the formation mechanism rather than on the technical details which can be found in Schicks et al.[52] and Priegnitz et al.[54]

The sediment sample with a diameter of 460 mm and a length of about 1300 mm can be set under simulated *in situ* conditions in the pressure vessel (1). The pore fluid pressure and confining pressure simulating the overburden is provided by ISCO syringe pumps, suitable for pressurization up to 25 MPa (2). The sample temperature is controlled by tempering and circulating the confining pressure fluid through a head exchanger (3). The heat exchanger is connected to a UNISTAT 510W circulation thermostat with a cooling power of 5 kW at 0 °C. A crucial component is the gas charging vessel (4). This is a temperature controlled pressure vessel containing a methane

E

dx.doi.org/10.1021/je5005609 | J. Chem. Eng. Data XXXX, XXX, XXX–XXX
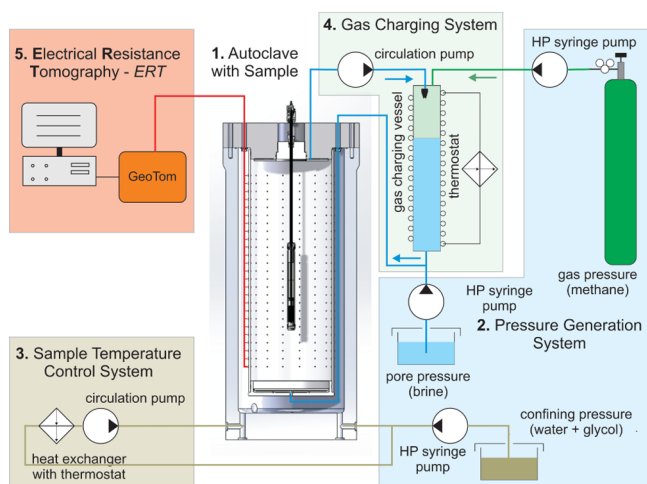
Figure 5. Five components of LARS: (1) temperature controlled pressure vessel with sediment sample; (2) pressure generation system with the high pressure syringe pumps (ISCO) for confining pressure fluid, gas, and pore water; (3) temperature control system for the pressure vessel with chiller, heat exchanger, and circulation pump for the confining pressure transfer fluid; (4) temperature-controlled gas charging pressure vessel with pore water circulation pump; (5) electrical resistivity tomography system. A detailed description of the functional principle and the hydrate formation procedure is given in the text.

headspace over pore water which is circulated through the sediment sample. The water is pumped from the sediment sample through a spray nozzle into the gas charging vessel. To avoid hydrate formation at the nozzle, the water is heated to a temperature slightly above hydrate stability (about 2 °C above the stability temperature for a given pressure) before it enters the gas charging vessel. The mist dissolves methane from the methane headspace and precipitates at the water surface. The methane-charged water flows back to the pressure vessel and enters the sediment sample with a temperature of about 1 to 2

°C above the hydrate stability. In the sediment sample, the water cools down to temperature conditions within the hydrate stability field and hydrate starts to form. Because the density of hydrate is lower than that of water, hydrate formation leads to a volume increase and therefore, a decrease of the methane headspace in the gas charging vessel. To account for that, water is withdrawn at certain time intervals from the system. Since dissolved salt ions are not incorporated into the hydrate structure during hydrate formation, the salt (NaCl) concentration of the remaining pore fluid increases with increasing hydrate saturation. From the corresponding electrical conductivity increase of withdrawn fluid samples, the amount of water fixed in the hydrate structure and the overall hydrate saturation can be determined.[15,22] The pore pressure is kept constant by a continuous methane supply from the methane cylinder via the methane pump.

The temperature measurements of the circulating fluid directly at the fluid inlet, outlet, and a number of different positions within the sample give an idea of the temperature field and its changes with increasing hydrate content. The assumption that the hydrate saturations in the sample are higher where the temperatures are the lowest and, thus, the driving force for hydrate growth is the highest, has not been supported by the first hydrate destabilization and methane production test carried out in this system.

The initial hydrate nucleation will very likely occur where the driving force or methane supersaturation respectively is highest and, therefore, the induction time is lowest.[55−58] But the subsequent hydrate growth process obviously is shifted along the gradient in methane concentration, against the flow direction, toward the stability boundary in the sediment sample. This hypothesis would explain the observation of high hydrate concentrations in the warmer parts of the sample and not as expected in the coldest areas.

To prove this hypothesis and to get a better understanding of the hydrate distribution within the sample the electrical resistivity tomography system (ERT) (5) with 375 electrodes
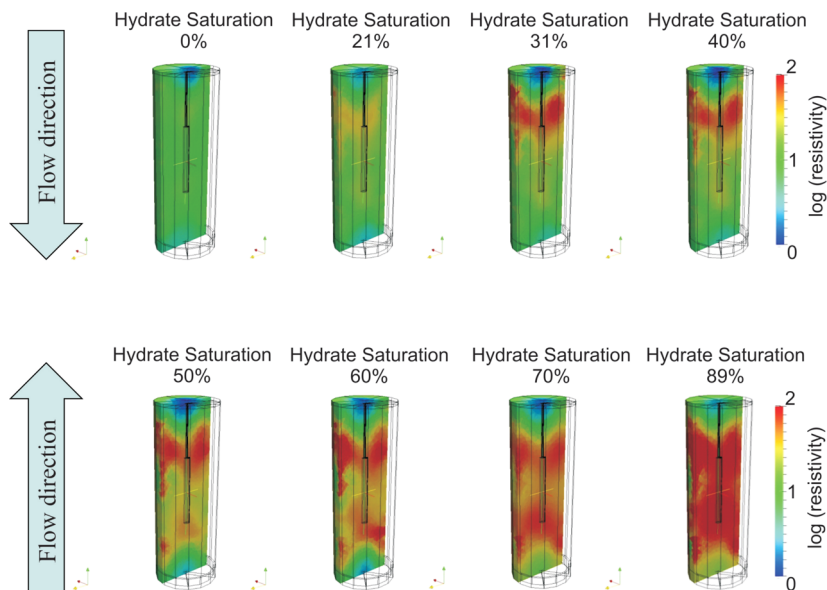

Figure 6. Evolution of the electrical resistivity distribution in the sediment sample during the hydrate formation phase. The color coded resistivity scale shows that areas with orange to red color represent high resistivity due to high concentration of pore space hydrate. At an overall hydrate concentration of 40 % the flow direction was changed from downward to upward in order to maintain fluid circulation with a low pore pressure gradient over the sample.

was installed and used.[54] ERT does not provide the high spatial resolution of X-ray and NMR tomography, but these highly resolving methods are not practicable for a pressure system with a sample volume of more than 200 L. Ultrasonic velocity tomography would have been another alternative, but for technical and budget reasons it could not be realized in our system yet.

3.3. Controls on Hydrate Saturation Distribution. The ERT provides images of the resistivity distribution inside the sediment sample, which can be transferred into a hydrate distribution using Archie's equation.[23] The ERT has been proven to be a very useful tool in an experiment aimed to simulate the 2008 depressurization experiment at Mallik.[16] To provide conditions close to that of the tested hydrate zone at Mallik, a hydrate saturation of about 90 % had to be produced in the sediment sample prior to the production test.[16] To realize such high hydrate saturation within a short time, it is important to maintain fluid circulation on high flow rates and low pressure gradients. On the basis of the ERT measurements we were able to assess where areas of high hydrate saturation start to form permeability barriers and could adjust the experimental conditions to avoid blockage. Figure 6 shows that we changed flow direction at a total hydrate saturation of about 40 % because hydrate was only accumulating in the upper third of the sample, which could be seen from the increasing resistivity.

The methane supply is another important issue producing high hydrate concentrations within a reasonable time. However, the performance of these hydrate formation systems mainly depends on the reached level of dissolved methane concentration.[53] To assess the performance of the system during this test, a commercial methane sensor was installed to measure the concentration of dissolved methane at the out- and inlet of the gas charging vessel. Figure 7 shows that the
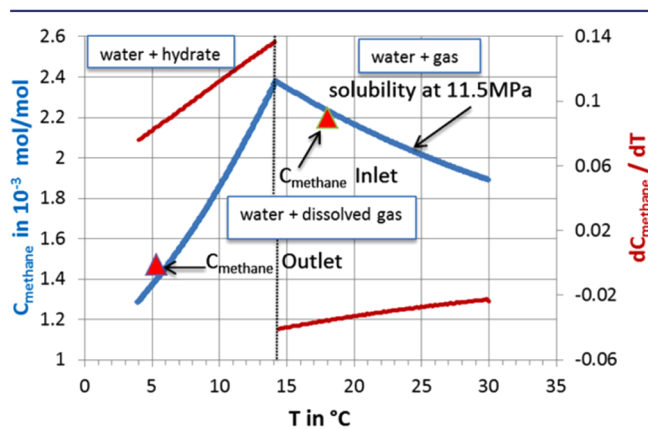
Figure 7. Methane solubility and change of methane solubility $(dC_{methane}/dT)$ with temperature at constant pressure of 11.5 MPa (calculations are based on equations published by Duan & Mao).[36] The red triangles represent methane concentration measurements of the water when it leaves the gas water charging vessel before it enters the sample (inlet) and after leaving the sample (outlet).

dissolved methane concentration is close to saturation when leaving the gas charging vessel, which is held at a temperature of 18 °C. The pore fluid is slightly oversaturated with respect to the lowest temperature in the sample when leaving the sediment at the fluid outlet.

The change of methane concentration with temperature $(dC_{methane}/dT)$ is highest directly when the water reaches the

hydrate stability and decreases with decreasing temperatures in the hydrate stability field. For flow velocities low enough for the hydrate formation process to consume all the available dissolved methane for the corresponding temperature, the highest hydrate concentrations should be observed directly in those areas of the sample where the water reaches the hydrate stability temperature. Almost all of the available, dissolved methane was consumed via hydrate formation within the time span the water percolates through the sediment. This information together with the observed saturation distribution from ERT and the temperature measurements inside the sediment sample (see Figure 8) proved that the hydrate concentration in the sediment is the highest where the change of methane concentration with temperature is the strongest. This is as one would expect if the hydrate growth kinetics is not limiting the process but the methane supply is the restricting factor.[53] Figure 8 shows that during the downward fluid flow about 60 % of the available methane should be consumed before reaching the temperature level of T4 in the upper third of the sample. About 40 % of the methane will be consumed in the remaining two-thirds of the sample. The ERT image at about 40 % total hydrate saturation supports the fact that the highest hydrate concentrations occur directly where the water enters the hydrate stability field slightly below temperature sensor T2. The bottom up flow changed the temperature field inside the sample because the warm water from the gas charging vessel now entered the system from the bottom. As a consequence this area was outside the hydrate stability field. At the position of T12, however, the pore water was already deep in the stability field and at the position of T6 more than 70 % of the available methane should be consumed due to hydrate formation. The ERT image taken at a hydrate saturation of about 89 % shows that we have the highest resistivities in the lower part of the upper third from the downward flow phase and in the upper part of the lower third from the upward flow phase. The resistivities in the middle part of the sample are a little bit lower.

The experiment shows clearly, that even on a short "lab-time-scale" hydrate forms with respect to the methane concentration along the stability curve as one would expect on a geological time scale in a natural hydrate system. Certainly, the nucleation starts somewhere deeper in the stability field. Since the water circulation causes high temperature gradients in the sample the initial supersaturation will vary depending on the location. Figure 8 reveals the possible level of supersaturation in relation to the temperature at different positions in the sample. Depending on the supersaturation and the corresponding induction time it is very likely that multiple nucleation occurs in the large sample volume. In a highly resolving NMR system such as NESSI used by Kossel et al.[59] the hydrate growth from the location of nucleation toward the direction of methane supply can be visualized.[60] However, we cannot resolve locations of nucleation with ERT in our experiment. Hydrate forms already according to the equilibrium stability conditions, when its concentration is high enough to produce a clear resistivity signature in the ERT-images. The hydrate growth along the concentration gradient toward the stability boundary is even on a lab-time-scale not a "slow" process.

3.4. Recrystallization and Aging. The extremely fast growth of pore space hydrate in the lab experiments compared to the natural scenarios very likely results in different crystal sizes and specific surfaces between the hydrate phase and the remaining pore water. Investigations on ice cores[61] showed that
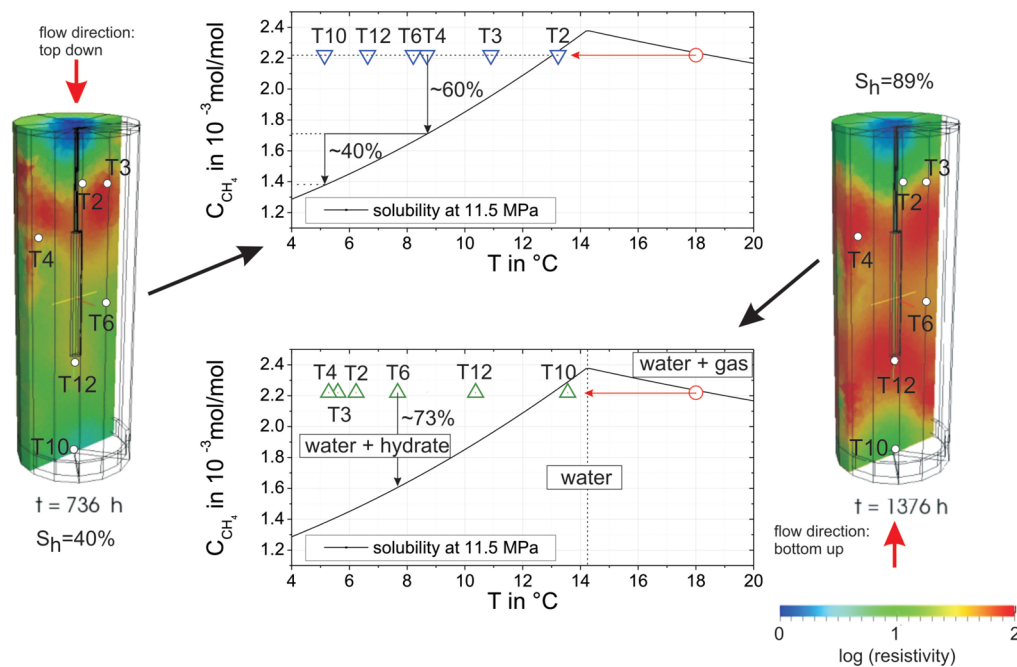
Figure 8. ERT images when flow direction was changed from top down to bottom up at an overall hydrate saturation of 40 % (left) and when the hydrate production phase was stopped at an overall hydrate saturation of 89 % (right). Switching the pore fluid flow direction changes the temperature field inside the sample which is shown in the diagrams for some selected temperature sensors. The upper diagram shows that about 60 % of the available methane should be consumed when reaching the temperature measured at position T4 in the lower part of the upper third. The lower diagram shows that about 70 % of the available methane is consumed before the temperature of T6 in the middle of the sample is reached.

a clear correlation exists between crystal size and the age of the ice core, indicating that even under natural conditions recrystallization is a process that needs to be considered. Klapp et al.[62] presented a study on the hydrate crystallite size distribution determined at six samples from the Gulf of Mexico and Hydrate Ridge. They report an increase of mean crystallite size with depth, possibly indicating a difference in the formation age. However, in our early experiments[15] we have clear evidence that recrystallization occurs as a time-dependent process. Figure 9 shows, for water saturations below 10 %, a slight but clear decrease of the electrical resistivity or the resistivity index with time and decreasing hydrate formation rate. The resistivity index here is simply the ratio of the electrical resistivites of the sample at certain hydrate saturation $\rho(S_h)$ and complete water saturation ρ_0 ($I = \rho(S_h)/\rho_0$). At very
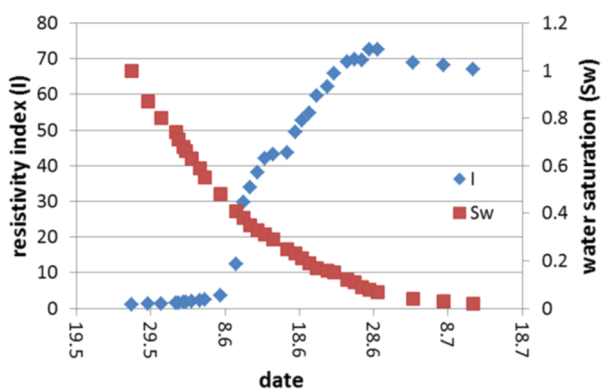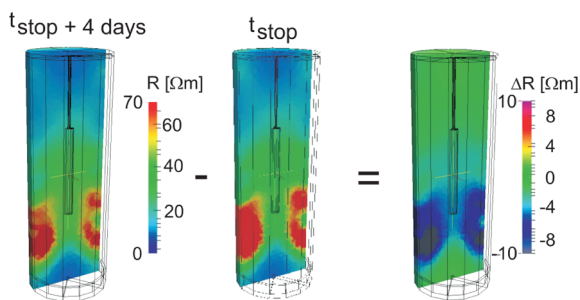
high hydrate saturations ($S_h > 90$ %), the hydrate formation rate strongly slows down because of the decline of the methane supply by water circulation. At this stage the resistivity index starts to decrease, although there still is a slight increase in hydrate saturation. We interpret this decrease as the result of a recrystallization due to Oswald ripening and a general equilibration of methane concentration gradients in the sample. The recrystallization process results in a "smoothing" of the fluid hydrate interface. The expression "smoothing" is used here as synonym for the reduction of the specific surface of the hydrate structure, the amount of micropores between hydrate crystals, the tortuosity, and the constrictions in the remaining fluid pathways. This, in turn, decreases the resistance to hydrated ion transport and so the electrical resistivity of the hydrate bearing sediment.

The change of resistivity index from the maximum value of $I = 72.6$ to the last measured value of $I = 67$ is about 8 % in 13 days.

Figure 10 shows that such a resistivity decrease due to recrystallization after hydrate formation was stopped could be confirmed in the LARS sample which has a volume that is 2200 times larger than the sample in the old system. Furthermore, the tomographic image shows that the effect is strongest where the resistivity and, therefore, the hydrate concentration is highest.

Figure 11 shows very simplified models of cylindrical pores containing pore filling hydrate in a coaxial arrangement to explain the observations and support our interpretation. The first of the three models shows a cylindrical pore containing a cylindrical hydrate core in the center. The hydrate core already underwent recrystallization. It is overgrown by small hydrate crystals forming a microporous layer that increases the surface of the water−hydrate interface. This microporous layer has the resistance R_{mp}. The free-pore water annulus around the

Figure 9. Increase of resistivity index and hydrate saturation ($S_h = 1 − S_w$) with time. The decrease of resistivity index with time for water saturations below 10 % is due to recrystallization processes of the pore-filling hydrate.

Figure 10. Tomographic resistivity images of a sample with 50 % hydrate saturation when the formation process was finished (t_{stop}), 4 days later ($t_{stop+4\ days}$), and the resulting differences in resistivity.
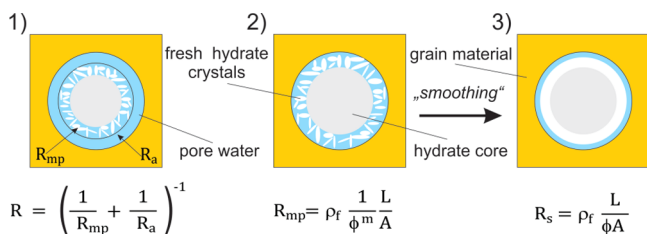
Figure 11. Pore models to explain the influence of recrystallization of fast grown hydrate crystallites on electrical resistivity. A detailed explanation is given in the text.

microporous hydrate layer has the resistance R_a. Since both resisters are in parallel, the resistance of the pore channel is mainly determined by the lower resistance of the fluid annulus at low-hydrate saturation. For increasing hydrate saturation the influence of R_{mp} increases. The second model shows the situation at very high hydrate saturation where the free-fluid annulus is vanished. The resistance of the pore channel is then R_{mp} which can be described by the Archie-equation as

$$R_{mp} = \rho_f \frac{1}{\Phi^m} \frac{L}{A} \qquad (1)$$

A is the cross sectional area of microporous layer, L is the length of the pore channel, Φ is the porosity of the microporous layer, and ρ_f is the fluid resistivity. In the third model we consider that recrystallization results in a smooth pore-free hydrate layer on the hydrate core. The resistance of the pore channel is

$$R_s = \rho_f \frac{L}{\Phi A} \qquad (2)$$

If we assume a microporosity of 0.5 and a standard cementation exponent of $m = 2$ the recrystallization from model 2 to model 3 would result in a resistance R_s of the smoothed system, which is the half of the original system with the resistance R_{mp}.

These models explain that "smoothing" can significantly decrease resistivity and support the observation that the effect is stronger as higher the hydrate saturation is.

4. CONCLUSION

The presented conceptual models for hydrate formation in sandy reservoirs suggest that all hydrate habits that we know from laboratory investigations on artificial hydrate-bearing samples occur in nature. However, the occurrence of cementing hydrate is probably restricted to (1) the BGHS in settings which are underlain by formations containing high methane gas concentrations and (2) reservoirs that contain free gas within

the hydrate stability field, for example, in areas with very high methane fluxes.

The main mechanism forming high concentrations of methane hydrate in sandy reservoirs is most likely from dissolved phase methane. The study of this hydrate formation process in the laboratory reveals that even under the very high formation rates compared to nature, this process is limited by methane supply rather than reaction kinetics.

The main differences to the natural systems result from the following facts:

(1) The hydrate formation rate sped up from about 1 % hydrate saturation increase in about 10^5 years according to the assumptions made in Rempel and Buffett[34] for natural scenarios to 1 to 2 % per day in the lab. This means that the time scale in nature is up to 5×10^7 times larger than that in the lab. The high hydrate formation rate is a result of the fast methane supply by fluid circulation. The Darcy-velocity of the circulating water is on the order of 1 mm/min (0.5 km/yr) compared to 0.3 mm/yr to 2 mm/yr for natural systems.[35]

(2) Temperature gradients in laboratory systems are orders of magnitude higher than that in natural systems. During the Mallik-2008 simulation in LARS, the fluid enters the sample at a temperature of about 13 °C and leaves it at about 5 °C. This corresponds to a temperature gradient of about 6 °C/m, which is more than 220 times higher than that in, for example, Mallik[63] (27 °C/km). In other words, the decrease in methane concentration that we observe over our sample occurs in Mallik at a depth interval of about 220 m within the hydrate stability field.

(3) The high temperature and methane concentration gradients in the lab sample result in high local hydrate growth rates, very likely producing a large number of small-sized hydrate crystallites that tend to recrystallize with time. From the observation of decreasing resistivities close to the end of the hydrate formation process we conclude a "smoothing" of the fluid- hydrate interface reducing the amount of pores between hydrate crystals, the tortuosity, and the constrictions of the charge carrier transport path ways. However, when the circulation is stopped at the end of an experiment, the system starts to equilibrate and the temperature and concentration gradients will decrease with time. Under equilibrated conditions Oswald ripening, driven by the concentration differences around crystals of different size, will be the main process of recrystallization in our lab-system. That Oswald ripening would finally result in patchy hydrate saturation as proposed by Dai et al.,[13] with patches containing 100 % hydrate in the pores embedded in hydrate-free water saturated sand, we can neither confirm nor refute based on our observations.

The recrystallization or "aging" effect requires more attention in future lab studies in order to assess its influence on the relationships between hydrate saturation and petrophysical sediment properties. Highly resolving visualization methods could be useful tools to study the recrystallization of pore filling hydrate. Kuhs et al.[64] report on a study based on synchrotron radiation X-ray cryo-tomography microscopy (SRXCTM) by which the nucleation and growth process of gas hydrate were observed in the presence of quartz grains and glass beads. SRXCTM under in situ conditions allows for the study of hydrate formation with a resolution sufficient to observe details of the interfaces involved in the recrystallization processes.

■ AUTHOR INFORMATION

Corresponding Author

*E-mail: erik@gfz-potsdam.de. Tel: ++49 (0)331 288 1276. Fax: ++49 (0)331 288 1450.

■ REFERENCES

(1) Sloan Jr, E. D.; Koh, C. *Clathrate Hydrates of Natural Gases*; CRC Press: Boca Raton, FL, 2007.

(2) Kvenvolden, K. A. Methane hydrate—A major reservoir of carbon in the shallow geosphere? *Chem. Geol.* **1988**, *71* (1), 41–51.

(3) Kvenvolden, K. A. A review of the geochemistry of methane in natural gas hydrate. *Org. Geochem.* **1995**, *23* (11), 997–1008.

(4) Milkov, A. V. Global estimates of hydrate-bound gas in marine sediments: How much is really out there? *Earth-Sci. Rev.* **2004**, *66* (3), 183–197.

(5) Archer, D.; Buffett, B.; Brovkin, V. Ocean methane hydrates as a slow tipping point in the global carbon cycle. *Proc. Int. Acad. Ecol. Environ. Sci.* **2009**, *106* (49), 20596–20601.

(6) Collett, T. S. Energy resource potential of natural gas hydrates. *AAPG Bull.* **2002**, *86* (11), 1971–1992.

(7) Makogon, Y. F.; Holditch, S. A.; Makogon, T. Y. Natural gas-hydrates—A potential energy source for the 21st Century. *J. Pet. Sci. Eng.* **2007**, *56* (1–3), 14–31.

(8) Boswell, R.; Collett, T. S. Current perspectives on gas hydrate resources. *Energy Environ. Sci.* **2011**, *4*, 1206–1215.

(9) Haeckel, M.; Suess, E.; Wallmann, K.; Rickert, D. Rising methane gas bubbles form massive hydrate layers at the seafloor. *Geochim. Cosmochim. Acta* **2004**, *68* (21), 4335–4345.

(10) Tréhu, A. M.; Long, P. E.; Torres, M. E.; Bohrmann, G.; Rack, F. R.; Collett, T. S.; Goldberg, D. S.; Milkov, A. V.; Riedel, M.; Schultheiss, P.; Bangs, N. L.; Barr, S. R.; Borowski, W. S.; Claypool, G. E.; Delwiche, M. E.; Dickens, G. R.; Gracia, E.; Guerin, G.; Holland, M.; Johnson, J. E.; Lee, Y. J.; Liu, C. S.; Su, X.; Teichert, B.; Tomaru, H.; Vanneste, M.; Watanabe, M.; Weinberger, J. L. Three-dimensional distribution of gas hydrate beneath southern Hydrate Ridge: Constraints from ODP Leg 204. *Earth Planet. Sci. Lett.* **2004**, *222* (3–4), 845–862.

(11) Bahk, J. J.; Kim, D. H.; Chun, J. H.; Son, B. K.; Kim, J. H.; Ryu, B. J.; Torres, M. E.; Riedel, M.; Schultheiss, P. Gas hydrate occurrences and their relation to host sediment properties: Results from Second Ulleung Basin Gas Hydrate Drilling Expedition. *East Sea. Mar. Pet. Geol.* **2013**, *47* (0), 21–29.

(12) Boswell, R.; Collett, T. S.; Frye, M.; Shedd, W.; McConnell, D. R.; Shelander, D. Subsurface gas hydrates in the northern Gulf of Mexico. *Mar. Pet. Geol.* **2012**, *34* (1), 4–30.

(13) Dai, S.; Santamarina, J. C.; Waite, W. F.; Kneafsey, T. J. Hydrate morphology: Physical properties of sands with patchy hydrate saturation. *J. Geophys. Res.: Solid Earth*, **2012**, *117*(B11).

(14) Boswell, R. Is gas hydrate energy within reach? *Science* **2009**, *325* (5943), 957–958.

(15) Spangenberg, E.; Kulenkampff, J.; Naumann, R.; Erzinger, J. Pore space hydrate formation in a glass bead sample from methane dissolved in water. *Geophys. Res. Lett.* **2005**, *32*.

(16) Uddin, M.; Wright, J. F.; Dallimore, S. R.; Coombe, D. Gas hydrate production from the Mallik reservoir: Numerical history matching and long-term production forecasting. In *Scientific results from the JOGMEC/NRCan/Aurora Mallik 2007−2008 Gas Hydrate Production Research Well Program, Mackenzie Delta, Northwest Territories, Canada*; Geological Survey of Canada, Bulletin 601; Dallimore, S. R., Yamamoto, K., Wright, J. F., Bellefleur, G., Eds.; Geological Survey of Canada: Ottawa, Canada, 2012; pp 261–289.

(17) Dai, J.; Snyder, F.; Gillespie, D.; Koesoemadinata, A.; Dutta, N. Exploration for gas hydrates in the deepwater, northern Gulf of Mexico: Part I. A seismic approach based on geologic model, inversion, and rock physics principles. *Mar. Pet. Geol.* **2008**, *25* (9), 830–844.

(18) Weitemeyer, K.; Constable, S. Mapping shallow geology and gas hydrate with marine CSEM surveys. *First Break* **2010**, *28* (6).

(19) Schwalenberg, K.; Haeckel, M.; Poort, J.; Jegen, M. Evaluation of gas hydrate deposits in an active seep area using marine controlled source electromagnetics: Results from Opouawe Bank, Hikurangi Margin, New Zealand. *Mar. Geol.* **2010**, *272* (1), 79–88.

(20) Waite, W. F.; Santamarina, J. C.; Cortes, D. D.; Dugan, B.; Espinoza, D.; Germaine, J.; Jang, J.; Jung, J.; Kneafsey, T. J.; Shin, H. Physical properties of hydrate-bearing sediments. *Rev. Geophys.* **2009**, *47* (4).

(21) Spangenberg, E. Modeling of the influence of gas hydrate content on the electrical properties of porous sediments. *J. Geophys. Res.: Solid Earth* **2001**, *106* (B4), 6535–6548.

(22) Spangenberg, E.; Kulenkampff, J. Influence of methane hydrate content on electrical sediment properties. *Geophys. Res. Lett.* **2006**, *33*(24).

(23) Archie, G. E. The electrical resistivity log as an aid in determining some reservoir characteristics. *Trans. AIMe* **1942**, *146* (1), 54–62.

(24) Schön, J. H. *Physical Properties of Rocks: Fundamentals and Principles of Petrophysics*; Pergamon: Oxford, UK 1996.

(25) Berge, L. I.; Jacobsen, K. A.; Solstad, A. Measured acoustic wave velocities of R11 (CCl3F) hydrate samples with and without sand as a function of hydrate concentration. *J. Geophys. Res.: Solid Earth* **1999**, *104* (B7), 15415–15424 (1978–2012).

(26) Yun, T. S.; Francisca, F. M.; Santamarina, J. C.; Ruppel, C. Compressional and shear wave velocities in uncemented sediment containing gas hydrate. *Geophys. Res. Lett.* **2005**, *32*(10).

(27) Dvorkin, J.; Nur, A. Acoustic signatures of patchy saturation. *Int. Jo. Solids Struct.* **1998**, *35* (34), 4803–4810.

(28) Voorhees, P. W. The theory of Ostwald ripening. *J. Stat. Phys.* **1985**, *38* (1–2), 231–252.

(29) Dvorkin, J.; Prasad, M.; Sakai, A.; Lavoie, D. Elasticity of marine sediments: Rock physics modeling. *Geophys. Res. Lett.* **1999**, *26* (12), 1781–1784.

(30) Chand, S.; Minshull, T. A.; Gei, D.; Carcione, J. M. Elastic velocity models for gas-hydrate-bearing sediments—A comparison. *Geophys. J. Int.* **2004**, *159* (2), 573–590.

(31) Haacke, R. R.; Westbrook, G. K.; Hyndman, R. D. Gas hydrate, fluid flow and free gas: Formation of the bottom-simulating reflector. *Earth Planet. Sci. Lett.* **2007**, *261* (3), 407–420.

(32) Fujii, T.; Noguchi, S.; Murray, D. R.; Takayama, T.; Fujii, K.; Yamamoto, K.; Dallimore, S. R.; Al-Jubori, A. Overview of wireline-logging analysis in the Aurora/JOGMEC/NRCCan Mallik 2L38 gas hydrate production research well. In *Scientific results from the JOGMEC/NRCan/Aurora Mallik 2007−2008 Gas Hydrate Production Research Well Program, Mackenzie Delta, Northwest Territories, Canada*; Geological Survey of Canada, Bulletin 601; Dallimore, S. R., Yamamoto, K., Wright, J. F., Bellefleur, G., Eds.; Geological Survey of Canada: Ottawa, Canada, 2012; pp 125–140.

(33) Ryu, B.-J.; Riedel, M.; Kim, J.-H.; Hyndman, R. D.; Lee, Y.-J.; Chung, B.-H.; Kim, I.-S. Gas hydrates in the western deep-water Ulleung Basin, East Sea of Korea. *Mar. Pet. Geol.* **2009**, *26* (8), 1483–1498.

(34) Rempel, A. W.; Buffett, B. A. Formation and accumulation of gas hydrate in porous media. *J. Geophys. Res.: Solid Earth (1978–2012)* **1997**, *102* (B5), 10151–10164.

J

dx.doi.org/10.1021/je5005609 | *J. Chem. Eng. Data* XXXX, XXX, XXX–XXX

(35) Xu, W.; Ruppel, C. Predicting the occurrence, distribution, and evolution of methane gas hydrate in porous marine sediments. *J. Geophys. Res.: Solid Earth* **1999**, *104* (B3), 5081–5095.

(36) Duan, Z.; Mao, S. A thermodynamic model for calculating methane solubility, density and gas phase composition of methane-bearing aqueous fluids from 273 to 523 K and from 1 to 2000 bar. *Geochim. Cosmochim. Acta* **2006**, *70* (13), 3369–3386.

(37) Osadetz, K. G.; Morrell, G. R.; Dixon, J.; Dietrich, J. R.; Snowdon, L. R.; Dallimore, S. R.; Majorowicz, J. A. Beaufort-Mackenzie Basin: A review of conventional and nonconventional (gas hydrate) petroleum reserves and undiscovered resources. *Geol. Surv. Can. Bull.* **2005**, *585*, 81.

(38) Hildenbrand, A.; Schlömer, S.; Krooss, B. Gas breakthrough experiments on fine-grained sedimentary rocks. *Geofluids* **2002**, *2* (1), 3–23.

(39) Geistlinger, H.; Krauss, G.; Lazik, D.; Luckner, L. Direct gas injection into saturated glass beads: Transition from incoherent to coherent gas flow pattern. *Water Resour. Res.* **2006**, *42*(7).

(40) Fauria, K. E.; Rempel, A. W. Gas invasion into water-saturated, unconsolidated porous media: Implications for gas hydrate reservoirs. *Earth Planet. Sci. Lett.* **2011**, *312* (1), 188–193.

(41) Donoghue, J. F. Sea level history of the northern Gulf of Mexico coast and sea level rise scenarios for the near future. *Clim. Change* **2011**, *107* (1–2), 17–33.

(42) Galushkin, Y. Numerical simulation of permafrost evolution as a part of sedimentary basin modeling: Permafrost in the Pliocene–Holocene climate history of the Urengoy field in the West Siberian basin. *Can. J. Earth Sci.* **1997**, *34* (7), 935–948.

(43) Liu, X.; Flemings, P. B. Passing gas through the hydrate stability zone at southern Hydrate Ridge, offshore Oregon. *Earth Planet. Sci. Lett.* **2006**, *241* (1), 211–226.

(44) Henry, P.; Thomas, M.; Clennell, M. B. Formation of natural gas hydrates in marine sediments: 2. Thermodynamic calculations of stability conditions in porous sediments. *J. Geophys. Res.: Solid Earth* **1999**, *104* (B10), 23005–23022.

(45) Malinverno, A. Marine gas hydrates in thin sand layers that soak up microbial methane. *Earth Planet. Sci. Lett.* **2010**, *292* (3), 399–408.

(46) Freer, E. M.; Sami Selim, M. Methane hydrate film growth kinetics. *Fluid Phase Equilib.* **2001**, *185* (1), 65–75.

(47) Spangenberg, E.; Beeskow-Strauch, B.; Luzi, M., Naumann, R.; Schicks, J. M.; Rydzy, M. *The process of hydrate formation in clastic sediments and its impact on their physical properties*. In Proceedings of the 6th International Conference on Gas Hydrates, Vancouver, July 6-20, 2008.

(48) Stoll, R. D.; Bryan, G. M. Physical properties of sediments containing gas hydrates. *J. Geophys. Res.: Solid Earth (1978–2012)* **1979**, *84* (B4), 1629–1634.

(49) Waite, W. F.; Winters, W. J.; Mason, D. H. Methane hydrate formation in partially water-saturated Ottawa sand. *Am. Mineral.* **2004**, *89* (8–9), 1202–1207.

(50) Priest, J. A.; Best, A. I.; Clayton, C. R., A laboratory investigation into the seismic velocities of methane gas hydrate-bearing sand *J. Geophys. Res.: Solid Earth (1978–2012)* **2005**, *110* (B4).

(51) Priest, J. A.; Rees, E. V.; Clayton, C. R.. Influence of gas hydrate morphology on the seismic velocities of sands. *J. Geophys. Res.: Solid Earth (1978–2012)* **2009**, *114* (B11).

(52) Schicks, J. M.; Spangenberg, E.; Giese, R.; Steinhauer, B.; Klump, J.; Luzi, M. New approaches for the production of hydrocarbons from hydrate bearing sediments. *Energies* **2011**, *4* (1), 151–172.

(53) Waite, W. F.; Spangenberg, E. Gas hydrate formation rates from dissolved-phase methane in porous laboratory specimens. *Geophys. Res. Lett.* **2013**, *40* (16), 4310–4315.

(54) Priegnitz, M.; Thaler, J.; Spangenberg, E.; Rücker, C.; Schicks, J. M. A cylindrical electrical resistivity tomography array for three-dimensional monitoring of hydrate formation and dissociation. *Rev. Sci. Instrum.* **2013**, *84* (10), 104502.

(55) Kashchiev, D.; Verdoes, D.; Van Rosmalen, G. M. Induction time and metastability limit in new phase formation. *J. Cryst. Growth* **1991**, *110* (3), 373–380.

(56) Kashchiev, D.; Firoozabadi, A. Driving force for crystallization of gas hydrates. *J. Cryst. Growth* **2002**, *241* (1), 220–230.

(57) Kashchiev, D.; Firoozabadi, A. Nucleation of gas hydrates. *J. Cryst. Growth* **2002**, *243* (3), 476–489.

(58) Kashchiev, D.; Firoozabadi, A. Induction time in crystallization of gas hydrates. *J. Crystal Growth* **2003**, *250* (3), 499–515.

(59) Kossel, E.; Deusner, C.; Bigalke, N.; Haeckel, M. Magnetic Resonance Imaging of Gas Hydrate Formation and Conversion at Sub-Seafloor Conditions. *Diffus. Fundam.* **2013**, *18* (15), 1–4.

(60) Kossel, E. GEOMAR, Helmholtz Centre for Ocean Research Kiel, Germany, personal communication, 2014.

(61) Gow, A. J.; Williamson, T. Rheological implications of the internal structure and crystal fabrics of the West Antarctic ice sheet as revealed by deep core drilling at Byrd Station. *Geol. Soc. Am. Bull.* **1979**, *87* (12), 1665–1677.

(62) Klapp, S. A.; Klein, H.; Kuhs, W. F., First determination of gas hydrate crystallite size distributions using high-energy synchrotron radiation. *Geophys. Res. Lett.* **2007**, *34*(13).

(63) Collett, T. S.; Dallimore, S. R. Quantitative assessment of gas hydrates in the Mallik L-38 Well, Mackenzie Delta, NWT, Canada. In Proceedings of the 7th International Conference on Permafrost, Yellowknife, Canada 1998.

(64) Werner, F.; Kuhs, W. F.; Chaouachi, M.; Falenty, A.; Sell, K.; Schwarz, J. O.; Wolf, M.; Enzmann, F.; Kersten, M.; Haberthüer, D. In-situ micro-structural studies of gas hydrate formation in sedimentary matrices. Proceedings of the 8th International Conference on Gas Hydrates (ICGH8–2014), Beijing, China, July 28–August 1, 2014.